Geophys. J. Int. (2004) **158,** 801–812 doi: 10.1111/j.1365-246X.2004.02336.x

How to choose a subset of frequencies in frequency-domain finite-difference migration

W. A. Mulder and R.-E. Plessix

Shell International E&P, PO Box 60, 2280 AB Rijswijk, the Netherlands

Accepted 2004 March 24. Received 2003 February 3; in original form 2003 April 14

SUMMARY

Finite-difference migration with the two-way wave equation can be accelerated by an order of magnitude if the frequency domain rather than the time domain is used. This gain is mainly accomplished by using a subset of the available frequencies. The implicit assumption is that the data have a certain amount of redundancy in the frequency domain.

The choice of frequencies cannot be arbitrary. If the frequencies are chosen with a constant increment and their spacing is too large, the well-known wrap-around that occurs when transforming back to the time domain will also show up in the migration to the depth domain, albeit in a more subtle way. Because migration involves propagation in a given background velocity model and summation over shots and receivers, the effects of wrap-around may disappear even when the Nyquist theorem is not obeyed.

We have studied these effects analytically for the constant-velocity case and determined sampling conditions that avoid wrap-around artefacts. The conditions depend on the velocity, depth of the migration grid and offset range. They show that the spacing between subsequent frequencies can be larger than the inverse of the time range prescribed by the Nyquist theorem. A 2-D example has been used to test the validity of these conditions for a more realistic velocity model. Finite-difference migration with the one-way wave equation shows a similar behaviour.

Key words: finite-differences, frequency domain, migration.

1 INTRODUCTION

Seismic imaging of complex earth structures is still a challenge in geophysics. The classic Kirchhoff and Born migration algorithms (Claerbout 1971; Beylkin 1985; Bleistein 1987; Docherty 1991) may fail when imaging near strong velocity variations and underneath hard layers. One of the difficulties is the complexity of the wave paths. Multivalued Kirchhoff migration has been proposed to improve the migration results and has led to better results when the background velocity is accurately known (ten Kroode *et al.* 1998; Xu & Lambaré 2000). Still, this method is based on the high-frequency approximation, which may be violated in complex earth structures.

The high-frequency approximation can be dropped by going from the eikonal and transport equations to the full two-way wave equation. The latter, however, has a large computational cost. This has prompted the development of approximate one-way factorizations of the wave equation that can be solved efficiently. Over the last decade, migration schemes based on the one-way wave equation have regained popularity (Wu 1994; Biondi & Palacharla 1996; Jin *et al.* 1998) because they seem to give better images beneath hard layers. However, because of the approximations made in the factorization, they tend to lose their accuracy at larger angles of incidence, away from the vertical, which seems to prevent them from correctly imaging steep dips. Again, these problems can be avoided by using the full two-way wave equation, discretised by a finite-difference or finite-element scheme. With the need for better imaging algorithms around complex structures and the continuous increase of computer power at low costs, these methods can be expected to become attractive in the near future.

Several authors have proposed to solve the two-way equation with finite-differences for the purpose of migration and velocity analysis (Symes & Carazzone 1991; Pratt 1999; Shin *et al.* 2001). The two-way equation can be solved either in the time domain or in the frequency domain. Both approaches should provide identical results. From a numerical point of view, modelling in the frequency domain can be more efficient for multishot surveys, at least in two space dimensions (Marfurt 1984). Also, attenuation is easily implemented in the frequency domain by using complex-valued velocities. The method is readily generalized from the constant-density acoustic to the fully acoustic and elastic case. Moreover, the grid spacing of the computational domain can be adapted to each frequency, meaning that we can use coarser grids for the lower frequencies.

When using the two-way wave equation for fitting observed data on the basis of a least-squares error functional, the frequency domain naturally lends itself to go from low to higher frequencies. In this setting, the least-squares functional is used for optimization of the background velocity model, which is iteratively updated to provide a better fit of the synthetic to the observed data. Because this functional has many local minima, the iterative process will often end prematurely. A scale approach, meaning that first the large-scale structures and then the smaller scale structures of the background model are determined, can reduce the chance of ending up in a local minimum (Bunks *et al.* 1995; Pratt 1999). Here the tacit assumption is that low temporal frequencies correspond to low spatial frequencies, which seems reasonable but is not necessarily true in general.

The least-squares functional may also be used for migration (Lailly 1983). The gradient or sensitivity of the functional with respect to the background model can be interpreted as a migration step. In this case, the higher frequencies are of interest. Iterative updates of the model can be performed to improve the data fit, providing a migration image that is close to true amplitude. The problem of local minima is avoided here by assuming that the migration velocity model is correct, that is, lies close to the global minimum of the error functional. Whether or not this is a realistic assumption needs to be verified afterwards.

When using the frequency domain for finite-difference migration, only a subset of the available frequencies may be used to reduce the computational effort (Plessix, Mulder & Pratt 2001; Plessix & Mulder 2002a). This assumes that there is some redundancy in the seismic data with respect to the frequencies.

The choice of frequencies cannot be arbitrary. Even for noise-free data, two criteria must be taken into account. The first is related to the resolution of reflectors in the migration image. Here the equivalent of Heisenberg's principle plays a role. The second criterion is Nyquist's theorem that is often applied to the sampling of time signals but is used here for sampling in the frequency domain. For regular time-series, the theorem gives the condition under which wrap-around, or aliasing or periodic repetition, can be avoided. Wrap-around may also show up in depth migration, albeit in a more subtle way. Because migration involves propagation in a given background velocity model and summation over shots and receivers, the effects of wrap-around may disappear even when the Nyquist theorem is not obeyed.

We have studied these effects analytically for the constant-velocity case and determined sampling conditions that avoid wrap-around artefacts. In Section 2, we use the high-frequency Born approximation in a constant-velocity model to study the gradient and Hessian of the least-squares functional. Minus the gradient is an unscaled migration image. The Hessian describes how reflectors are mapped via the data domain back to the spatial domain, *cf.* Pratt *et al.* (1998). If the Hessian is or is close to a diagonal operator, the product of its inverse and minus the gradient of the least-squares functional represents a true-amplitude migration image (Plessix & Mulder 2004). Artefacts occur in the migration image when the Hessian is non-invertable. Here we consider the special case in which the Hessian is singular because of repetitive structures caused by the choice of frequencies. We have determined conditions that prevent the occurrence of these artefacts. The analysis also predicts where artefacts will occur if these conditions are violated.

A 2-D finite-difference example of frequency-domain migration with the two-way wave equation has been used in Section 3 to test the validity of these conditions for a more realistic velocity model. A one-way wave equation example shows a similar behaviour.

2 ANALYTICAL STUDY

2.1 Main result

We start with the main result of this section, which can be derived by simple arguments. This will be followed by a more rigorous derivation of where artefacts can occur.

Consider zero-offset data of time length T recorded at zero depth and a model with constant velocity V and maximum depth $z_{\max} = \frac{1}{2}T/V$. The Nyquist criterion states that wrap-around or repetitions in the time domain and hence the depth domain can be avoided for a frequency spacing $\Delta f \leq \Delta f^0_{\max}$, where

$$\Delta f^0_{\max} = 1/T = \tfrac{1}{2}V/z_{\max}. \tag{1}$$

If a range of offsets is considered, the upper bound will change as a result of the familiar wavelet stretch with offset in common image gathers. Given a single trace at fixed offset $2h$, the minimum arrival time for a reflector at almost zero depth will approach $T_{\min} = 2h/V$. The maximum arrival time will be $T_{\max} = 2\sqrt{z^2_{\max} + h^2}/V$ for a reflector at maximum depth $z_{\max}$. The result is a bound

$$\Delta f^h_{\max} = 1/(T_{\max} - T_{\min}) = \frac{1}{2}\frac{V}{\sqrt{z^2_{\max}+h^2}-h}. \tag{2}$$

Below, we will give a more rigorous derivation of this formula by examining the conditions for which the Hessian is singular. This will also allow us to predict where artefacts will occur. For simplicity, the derivation is carried out for a constant-velocity model and only uses travel times.

In the following, we will list the equations used in the analysis. Next, we consider a 1-D reflectivity model for the case of a single offset, with the zero-offset case as a special case. In the examples, sources and receivers are placed at zero depth. Then, we proceed with multi-offset data, followed by some remarks on 2-D reflectivity models.

Apart from artefacts, the choice of the range of frequencies will affect the resolution of the reflectors. This is related to Heisenberg's principle. Because there is a substantial body of literature on improving the resolution of reflectors by careful pre-processing, windowing, tapering and weighting, we only give the most basic description of this subject in Section 2.6.

2.2 Basic equations

Let $\mathbf{x}$ be a scattering point of the subsurface and $\mathbf{x}_S$ and $\mathbf{x}_R$ the source and receiver positions. The reflectivity on a computational grid is denoted by $\mathrm{r}(\mathbf{x})$. In the frequency domain, the high-frequency approximation and the Born approximation result in a synthetic seismogram

$$c(\mathbf{x}_S, \mathbf{x}_R, \omega; \mathrm{r}) = \sum_{\mathbf{x}} \mathrm{r}(\mathbf{x}) e^{i\omega\tau(\mathbf{x}_S,\mathbf{x}_R,\mathbf{x})} s(\omega), \tag{3}$$

with ω the angular frequency. The sum of the travel times from the source to the subsurface point and from the subsurface point to the receiver is $\tau(\mathbf{x}_S, \mathbf{x}_R, \mathbf{x})$. The source function or wavelet is s. The summation is carried out over all scattering points. The amplitudes are not taken into account for simplicity.

The goal of migration or imaging is to find the reflectivity from the seismic data in a given smooth background velocity model. In the present setting, this implies that the travel times are known. Migration can be formulated as an inverse problem. Let d be the observed data. Imaging amounts to minimization of the cost function

$$J(\mathrm{r}) = \frac{1}{2} \sum_{\omega} \sum_{\mathbf{x}_S,\mathbf{x}_R} |c(\mathbf{x}_S, \mathbf{x}_R, \omega; \mathrm{r}) - d(\mathbf{x}_S, \mathbf{x}_R, \omega)|^2. \tag{4}$$

The (negative of) the gradient of this cost function with respect to the reflectivity is similar to classic migration (Lailly 1983; Tarantola 1984). Migration weights can be obtained by constructing a suitable approximation to the inverse of the Hessian (Plessix & Mulder 2002b, 2004). In the current example, the gradient $g = \frac{\partial J}{\partial \mathrm{r}}$ is given by

$$g(\mathbf{x}) = \mathrm{Re}\left\{ \sum_{\omega} \sum_{\mathbf{x}_S,\mathbf{x}_R} e^{-i\omega\tau(\mathbf{x}_S,\mathbf{x}_R,\mathbf{x})} \bar{s}(\omega)[c(\mathbf{x}_S, \mathbf{x}_R, \omega; \mathrm{r}) - d(\mathbf{x}_S, \mathbf{x}_R, \omega)] \right\}, \tag{5}$$

where Re denotes the real part of a complex number and $\bar{s}$ the conjugate of s.

In the following, it will prove useful to study the Hessian, H, of the cost function,

$$\mathrm{H}(\mathbf{x}, \mathbf{x}') = \mathrm{Re}\left\{ \sum_{\omega} \sum_{\mathbf{x}_S,\mathbf{x}_R} |s(\omega)|^2 e^{i\omega[\tau(\mathbf{x}_S,\mathbf{x}_R,\mathbf{x}) - \tau(\mathbf{x}_S,\mathbf{x}_R,\mathbf{x}')]} \right\}. \tag{6}$$

In the current linear example, the gradient obeys $g(\mathbf{x}) = \sum_{\mathbf{x}'} \mathrm{H}(\mathbf{x}, \mathbf{x}')[\mathrm{r}(\mathbf{x}') - \tilde{\mathrm{r}}(\mathbf{x}')]$ if the observed data $d(\mathbf{x}_S, \mathbf{x}_R, \omega) = c(\mathbf{x}_S, \mathbf{x}_R, \omega; \tilde{\mathrm{r}})$ have been obtained from a given reflectivity $\tilde{\mathrm{r}}$. Clearly, the minimization of J will recover $\tilde{\mathrm{r}}$ only if H is invertible.

Two obvious types of artefact may be expected. First, if only one shot and one receiver are considered, we have $\mathrm{H}(\mathbf{x}, \mathbf{x}') \neq 0$ for $\tau(\mathbf{x}_S, \mathbf{x}_R, \mathbf{x}') = \tau(\mathbf{x}_S, \mathbf{x}_R, \mathbf{x})$. The curves with constant $\tau(\mathbf{x}_S, \mathbf{x}_R, \mathbf{x})$ are the familiar migration smiles. Summing over many source–receiver pairs will generally remove these smiles in accordance with the principle of stationary phase. Secondly, a large spacing between subsequent frequencies may produce artefacts resembling wrap-around or periodic repetition. Repetitive patterns in the Hessian occur if there are two scattering points $\mathbf{x}$ and $\mathbf{x}_1 \neq \mathbf{x}$ obeying

$$\mathrm{H}(\mathbf{x}_1, \mathbf{x}') = \mathrm{H}(\mathbf{x}, \mathbf{x}') \quad \forall\, \mathbf{x}'. \tag{7}$$

This will cause the Hessian to be singular.

2.3 Single-offset case

Consider a single trace and a 1-D model, so that the reflectivity $\mathrm{r} = \mathrm{r}(z)$. The distance (offset) between the source and the receiver is $2h$. Because only one trace is considered, there is a one-to-one map between the time domain and the depth domain, namely $z = \sqrt{(\frac{1}{2}Vt)^2 - h^2}$. The scattering point is fully determined by its depth, z. Using eq. (6) describing the Hessian, the condition in eq. (7) becomes

$$\cos\left\{\frac{2\omega}{V}[\mathrm{dist}(z_1) - \mathrm{dist}(z')]\right\} = \cos\left\{\frac{2\omega}{V}[\mathrm{dist}(z) - \mathrm{dist}(z')]\right\} \quad \forall z' \forall \omega, \tag{8}$$

where $\mathrm{dist}(z) = \sqrt{z^2 + h^2}$ is the distance between the source or receiver and the subsurface point. This relation leads to two possibilities:

$$\begin{aligned} \frac{2\omega}{V}[\mathrm{dist}(z_1) - \mathrm{dist}(z')] &= \frac{2\omega}{V}[\mathrm{dist}(z) - \mathrm{dist}(z')] + 2n\pi, \\ \frac{2\omega}{V}[\mathrm{dist}(z_1) - \mathrm{dist}(z')] &= -\frac{2\omega}{V}[\mathrm{dist}(z) - \mathrm{dist}(z')] + 2n\pi, \end{aligned} \tag{9}$$

for an integer n. In the second relation, z_1 depends on z'. Therefore, in general, this relation cannot be satisfied for all z'. Assuming $\omega = 2q\pi\Delta f$ and replacing n by qp where q and p are two integers, the first relation leads to

$$z_1 = \sqrt{\left(\sqrt{z^2 + h^2} + \frac{pV}{2\Delta f}\right)^2 - h^2}. \tag{10}$$

Artefacts occur if there is an integer p such that z_1 is in the migrated image, i.e. if $z_1 \in [0, z_{\max}]$. Note that z_1 depends on h but not on ω and z'.

Eq. (10) can be inverted to find the largest frequency spacing that avoids artefacts. In this way, we obtain the frequency interval

$$\Delta f^h_{\max} = \frac{V}{2\left(\sqrt{z^2_{\max} + h^2} - h\right)}, \tag{11}$$

which will be referred to as the offset frequency spacing. For the zero-offset case, we recover the Nyquist frequency spacing $\Delta f^0_{\max}$ of eq. (1).

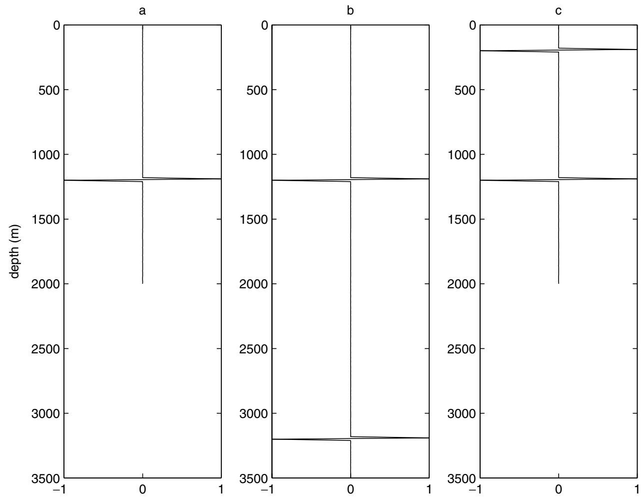

Figure 1. Migration results of zero-offset data with a true event at 1.2 km, using (a) $\Delta f = 0.5$ Hz and a migration depth of 2 km, (b) $\Delta f = 0.5$ Hz and a migration depth of 3.5 km and (c) $\Delta f = 1.0$ Hz and a migration depth of 2 km.

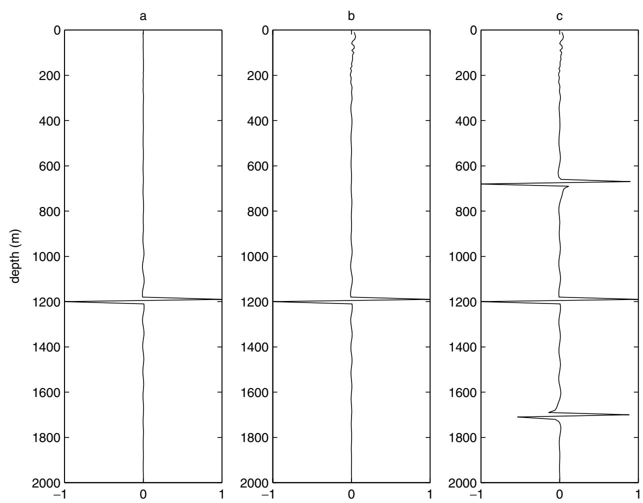

Figure 2. Migration results for 500-m offset data with a true event at 1.2 km, using (a) $\Delta f = 0.5$ Hz, (b) $\Delta f = 1.0$ Hz and (c) $\Delta f = 2.0$ Hz.

As an illustration of eq. (10), we consider a 1-D model of 2-km depth with a reflector at 1.2-km depth and a velocity $V = 2000$ m s^{-1}. The maximum time is 2 s and the Nyquist frequency spacing is 0.5 Hz.

First, we consider the zero-offset case. The results are shown in Fig. 1. If the migration depth $z_{\max} = \frac{1}{2} V T_{\max} = 2$ km and the frequency spacing $\Delta f^0_{\max} = 0.5$ Hz, we obtain the result shown in Fig. 1(a). No wrap-around occurs. The migration depth is in agreement with the maximum time and the frequency spacing is the one dictated by the Nyquist criterion. Next, if a migration depth of 3.5 km is used with a frequency spacing of 0.5 Hz, an artefact can be seen in the migrated image of Fig. 1(b) at 3.2 km depth, which corresponds to $p = 1$ in eq. (10). The migration depth is too large because the data do not contain information from depths beyond 2 km; we obtain a periodic result. For $\Delta f = 1.0$ Hz and a migration depth of 2 km, an artefact at 0.2 km can be seen in Fig. 1(c), which corresponds to $p = -1$. The frequency spacing is too large to correctly represent the data.

Next, a trace at 500-m offset is considered. The offset frequency spacing is $\Delta f^h_{\max} = 0.57$ Hz. For $\Delta f = 0.5$ Hz, the result is shown in Fig. 2(a). The reflectivity is correctly recovered, as expected. For $\Delta f = 1.0$ Hz, we obtain the result shown in Fig. 2(b). No artefacts appear and the reflectivity is correctly recovered even if the frequency spacing is higher than the offset frequency spacing. In this special case, it is not possible to find a $p \neq 0$ such that z_1 is in the interval [0, 2] km. In fact, if we use $z_{\max} = 1.2$ km instead of $z_{\max} = 2$ km, we find an offset frequency spacing of 1.02 Hz. Therefore, we can get away with a $\Delta f = 1.0$ Hz because of the absence of reflectors below 1.2 km. For $\Delta f = 2.0$ Hz, two artefacts occur in Fig. 2(c), one at $z = 681$ m ($p = -1$) and one at $z = 1708$ m($p = 1$).

2.4 Multi-offset case

Eq. (10) shows that the wrap-around artefacts depend on offset. Their amplitudes will decrease when a stack over the offsets is performed. This is illustrated in Figs 3 and 4. The amplitudes of the artefacts decrease relatively to the amplitudes of the true event when the number of traces increases.

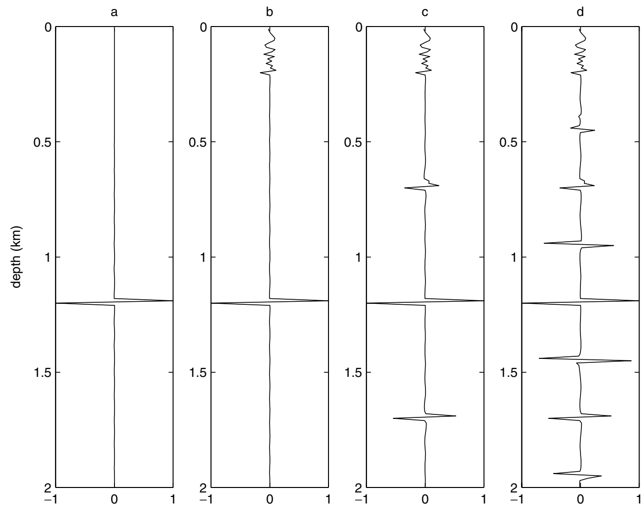

Figure 3. Migration images for multi-offset data with a true event at 1.2 km. The offsets range from 0 to 500 m with a spacing of 50 m. The frequency spacings are (a) $\Delta f = 0.5$ Hz, (b) $\Delta f = 1.0$ Hz, (c) $\Delta f = 2.0$ Hz and (d) $\Delta f = 4.0$ Hz.

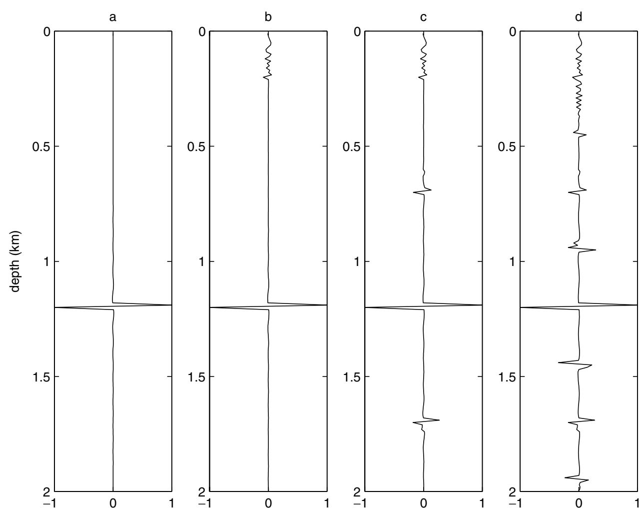

Figure 4. Migration images for multi-offset data with a true event at 1.2 km. The offsets range from 0 to 1000 m with a spacing of 50 m. The frequency spacings are (a) $\Delta f = 0.5$ Hz, (b) $\Delta f = 1.0$ Hz, (c) $\Delta f = 2.0$ Hz and (d) $\Delta f = 4.0$ Hz.

Eq. (10) was obtained from the condition of singularity of the Hessian. This condition is offset-dependent, meaning that with multi-offset data the Hessian is likely no longer singular. Numerically, the artefacts still exist because the migration is just the first step of the inversion, namely minus the gradient of the cost function evaluated at the initial guess. The full minimization of the cost function has yet to be performed. Moreover, the Hessian may have a very large condition number. If this condition number is too large, the Hessian is numerically not invertible. If the condition number is small enough, the wrap-around that appears in the gradient can be suppressed by minimization of the cost function given in eq. (4).

In practice, the Hessian is hardly ever directly used because of its size and high computational cost. Instead, an iterative method that only needs the gradient can be applied to minimize the cost function. The convergence rate of the iterative scheme can be accelerated by pre-conditioning with a diagonal matrix that is an approximation of the full Hessian (Plessix & Mulder 2002b, 2004).

In the present example, the Hessian and its condition number are readily computed. We expect that an iterative method will lead to an improvement of the migration image if the Hessian has a reasonable condition number. The condition number of the Hessian is plotted in Fig. 5 as a function of the maximum offset in the data, using a range of offsets starting at zero with a 50-m increment. The Hessian is assumed to be regular for a condition number around 100 and ill-posed for much larger values. For condition numbers exceeding 10^{16}, we cannot numerically distinguish between an ill-conditioned or singular problem. From Fig. 5, we infer that an iterative scheme is likely to provide the correct reflectivity if the maximum offset exceeds 1400 m for a frequency spacing $\Delta f = 4$ Hz, 800 m for $\Delta f = 2$ Hz, 300 m for $\Delta f = 1.0$ Hz and of course 0 m for $\Delta f = 0.5$ Hz.

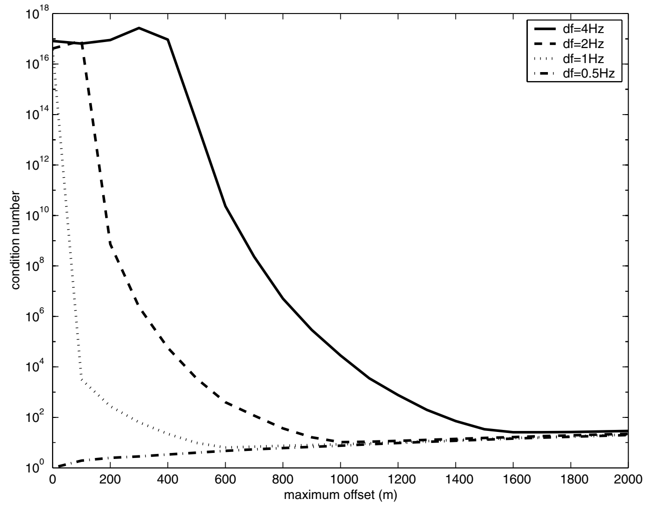

Figure 5. Condition number of the Hessian as a function of the maximum offset for different frequency spacings.

2.5 Two-dimensional model

The analysis of the Hessian can be extended to a 2-D reflector model. The wrap-around condition in eq. (7) then becomes

$$\cos\{\omega[\tau(\mathbf{x}_\mathrm{S}, \mathbf{x}_\mathrm{R}, \mathbf{x}_1) - \tau(\mathbf{x}_\mathrm{S}, \mathbf{x}_\mathrm{R}, \mathbf{x}')]\} = \cos\{\omega[\tau(\mathbf{x}_\mathrm{S}, \mathbf{x}_\mathrm{R}, \mathbf{x}) - \tau(\mathbf{x}_\mathrm{S}, \mathbf{x}_\mathrm{R}, \mathbf{x}')]\}. \tag{12}$$

This condition should hold for all $\mathbf{x}'$ and ω, leading to

$$\tau(\mathbf{x}_\mathrm{S}, \mathbf{x}_\mathrm{R}, \mathbf{x}_1) = \tau(\mathbf{x}_\mathrm{S}, \mathbf{x}_\mathrm{R}, \mathbf{x}) + 2\frac{p}{\Delta f}, \tag{13}$$

with integer p. For a constant velocity, the condition in eq. (13) becomes

$$\begin{aligned} &\sqrt{(x_1 - x_S)^2 + (z_1 - z_S)^2} + \sqrt{(x_1 - x_R)^2 + (z_1 - z_R)^2} = \\ &\quad \sqrt{(x - x_S)^2 + (z - z_S)^2} + \sqrt{(x - x_R)^2 + (z - z_R)^2} + 2p\frac{V}{\Delta f}. \end{aligned} \tag{14}$$

These curves are ellipses with foci at the source and receiver positions. For $p = 0$, the curves correspond to the classic migration smiles. The wrap-around artefacts have the same behaviour. The stack over the sources and the receivers will reduce the effects of the wrap-around artefacts. This is illustrated in Fig. 6, where the true event is at 1.2-km depth. The artefacts are different for different source and receiver pairs and do not stack constructively.

2.6 Resolution

So far, we have only considered artefacts related to wrap-around that are determined by the choice of the frequency spacing Δf. The range of frequencies should also be taken into account because it defines the resolution of the reflectors. This is related to Heisenberg's principle.

The following textbook example illustrates the type of artefacts that may occur. If we add $M + 1$ frequencies in a fixed range with a constant frequency spacing, we obtain

$$\sum_{m=0}^{M} \cos\left[2\pi(f_\mathrm{min} + m\Delta f)t\right] = \cos\left[2\pi\tfrac{1}{2}(f_\mathrm{min} + f_\mathrm{max})t\right] \frac{\sin[\pi(f_\mathrm{max} - f_\mathrm{min} + \Delta f)t]}{\sin(\pi\Delta f t)}. \tag{15}$$

Here $f_\mathrm{max} = f_\mathrm{min} + M\Delta f$. The resolution of the wave packet is determined by the main lobe of the sine factor on the right-hand side, which for small Δf leads to the familiar Heisenberg relation $\Delta t^\mathrm{res} = 1/(f_\mathrm{max} - f_\mathrm{min})$, apart from an $O(1)$ constant. The cosine factor on the right-hand side is the carrier wave. It has a mean frequency $\frac{1}{2}(f_\mathrm{min} + f_\mathrm{max})$ and a corresponding time interval $\Delta t^\mathrm{carrier} = 1/(f_\mathrm{min} + f_\mathrm{max})$. If Δt^res is considerably larger than $\Delta t^\mathrm{carrier}$, there will be several oscillations inside the interval Δt^res that might be interpreted as artefacts.

This example can be translated to a migration setting by assuming a 1-D reflectivity model and constant velocity. If there is a single reflector at depth z_1, the data are given by

$$d(h, \omega) = \tilde{r}(z_1)e^{i\omega\tau(h,z_1)}. \tag{16}$$

The source spectrum has been dropped for simplicity. We can do the summation of the gradient in eq. (5) in the same way as in eq. (15) or, for a change, replace the summation by an integration over the frequency range $[f_\mathrm{min}, f_\mathrm{max}]$. In the latter case, we obtain

$$g(z) = 2\cos\left[\pi(f_\mathrm{max} + f_\mathrm{min})\Delta\tau(z)\right]\frac{\sin\left[\pi(f_\mathrm{max} - f_\mathrm{min})\Delta\tau(z)\right]}{\Delta\tau(z)}, \tag{17}$$

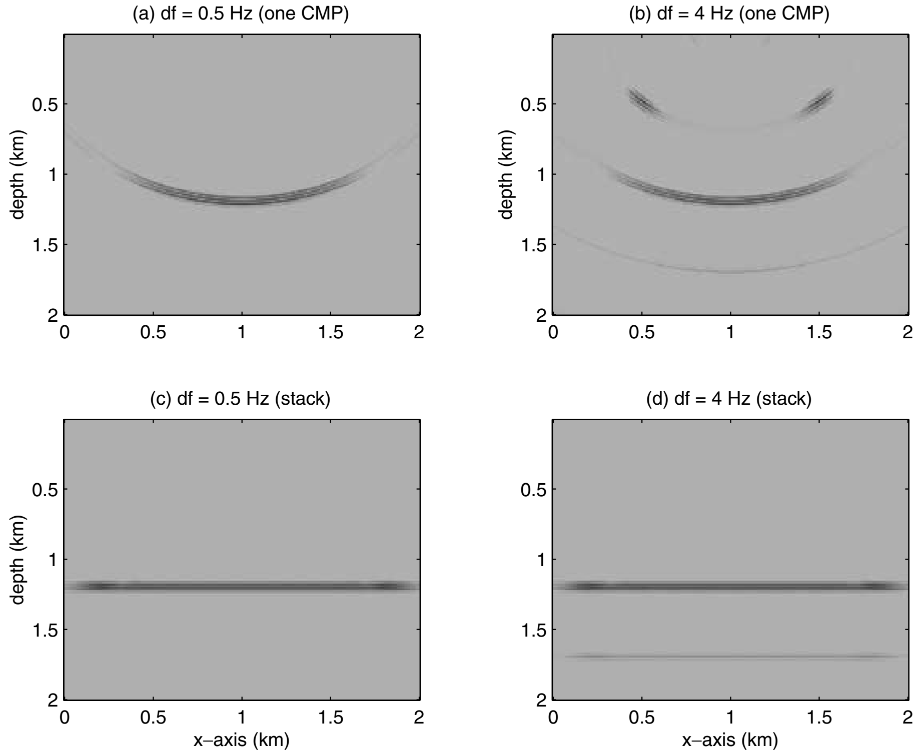

Figure 6. Migration result for one common mid-point (CMP) when (a) $\Delta f = 0.5$ Hz and (b) $\Delta f = 4.0$ Hz. Stack of 100 CMPs when (c) $\Delta f = 0.5$ Hz and (d) $\Delta f = 4$ Hz.

with $\Delta\tau(z) = \tau(h, z) - \tau(h, z_1)$. The gradient $g(z)$ is the product of a slowly oscillating envelope and a rapid carrier wave. As before, the resolution Δz^{res} is given by the main lobe of the slowly oscillating function

$$\pi(f_{\max} - f_{\min})\Delta\tau(z_1 + \Delta z^{\mathrm{res}}) = \pi \quad \text{or} \quad \Delta\tau(z_1 + \Delta z^{\mathrm{res}}) = \frac{1}{f_{\max} - f_{\min}}. \tag{18}$$

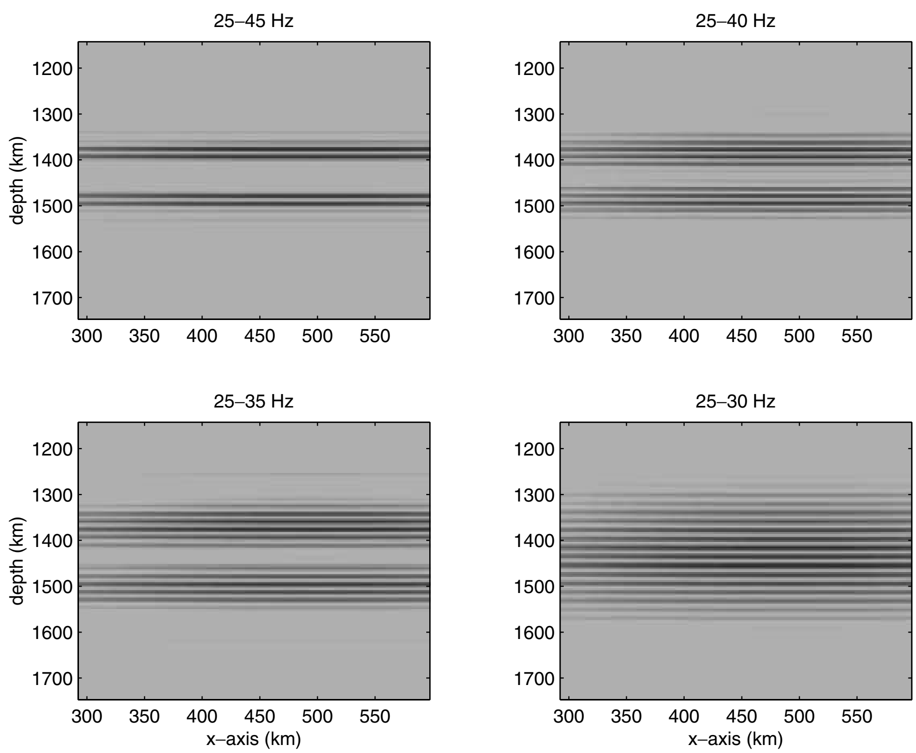

Figure 7. Resolution for different frequency ranges.

In a constant-velocity model and with the assumption that $\Delta z^{\mathrm{res}} \ll \sqrt{z_1^2 + h^2}$, the resolution for a data trace with offset $2h$ becomes

$$\Delta z^{\mathrm{res}} \simeq \frac{1}{2}\sqrt{1 + (h/z_1)^2}\,\frac{V}{f_{\max} - f_{\min}}. \tag{19}$$

Clearly, the best resolution is obtained for the zero-offset trace. The wavelength of the carrier wave $\Delta z^{\mathrm{carrier}}$ is given by the main lobe of the rapidly oscillating function:

$$\Delta z^{\mathrm{carrier}} \simeq \frac{1}{2}\sqrt{1 + (h/z_1)^2}\,\frac{V}{f_{\max} + f_{\min}}. \tag{20}$$

To illustrate this result, we take the same example as before, but now with two reflectors at 1.4- and 1.5-km depth in a constant-velocity model with the velocity V equal to 2000 m s^{-1}. The results are shown Fig. 7. In the first example, a frequency range from 25 to 45 Hz has been used, giving a resolution of $\Delta z^{\mathrm{res}} = 33$ m. The two reflectors are well imaged. Next, a frequency range of 25–35 Hz is used, giving a resolution of 100 m. It is still possible to distinguish the two discontinuities. Finally, a frequency range from 25 to 30 Hz is used, with a resolution $\Delta z^{\mathrm{res}} = 200$ m. Now, the two discontinuities cannot be distinguished any more.

3 TWO-DIMENSIONAL SYNTHETIC EXAMPLE

The analysis presented above is based on a constant-velocity model and provides guidelines for choosing the frequency spacing and range. Here we test the validity of these conditions for a more realistic velocity model. A representative average value of the velocity is used in the earlier formulae.

The velocity model is that of the SEG/EAGE salt model (Aminzadeh *et al.* 1997). Using a time-domain finite-difference code (Mulder & Plessix 2002), 237 shots of 65 receivers were generated with a maximum recording time of 5 s. These data were processed by blanking the direct arrival and truncating the recording time to 4 s before transforming to the frequency domain. The acquisition geometry mimics a marine acquisition with a shot every 80 m and with a 40-m spacing between receivers. The maximum offset is 2.7 km. The maximum depth in the model used to generate the data is 4.2 km. The velocity model and the shortest-offset data are displayed in Figs 8 and 9, respectively.

In this example, the frequency ranges from 6 to 26 Hz. The resolution, as given in eq. (19), is around 100 m at 2.7-km depth. Because 4 s of data have been used, the Nyquist frequency spacing is 0.25 Hz. The offset frequency spacing, as defined in eq. (11), equals 0.3 Hz for the maximum offset, assuming a velocity of 2000 m s^{-1}, which corresponds to the average velocity of the sediments. In this example, the ratio between the maximum offset and the maximum depth is 0.6, which is rather small. This is why the optimal frequency sampling is close to the classic Nyquist frequency sampling.

The data were processed by frequency-domain finite-difference migration for the full two-way wave equation (Marfurt 1984; Pratt 1999) and also for the one-way wave equation (Collino & Joly 1995). Migration images were computed with four different frequencies samplings: 0.3, 0.5, 1.0 and 2.0 Hz. Figs 10 and 11 display the two-way and one-way migration results for $\Delta f = 0.3$ Hz. Both images are almost free of artefacts, thereby validating the formulae. Even if the noise increases with increasing frequency spacing, a frequency spacing of 0.5 Hz still provides a reasonable image as can be seen in Figs 12 and 13. If the frequency spacing becomes too large, spurious layers appear in the images as shown in Figs 14, 15, 16 and 17. Note that for a migration with a frequency sampling of 1 Hz, there are no artefacts between 0- and 2-km depth. This corresponds to approximately 2 s of data and a Nyquist frequency of 0.5 Hz. However, the optimal frequency sampling as defined in eq. (11) gives 0.94 Hz, with a maximum depth of 2 km and a maximum offset of 2.7 km. This explains why there are no artefacts at less than 2-km depth. Eqs (10) and (11) not only define the optimal frequency sampling, but also help to interpret the migrated images and determine where the wrap-around occurs.

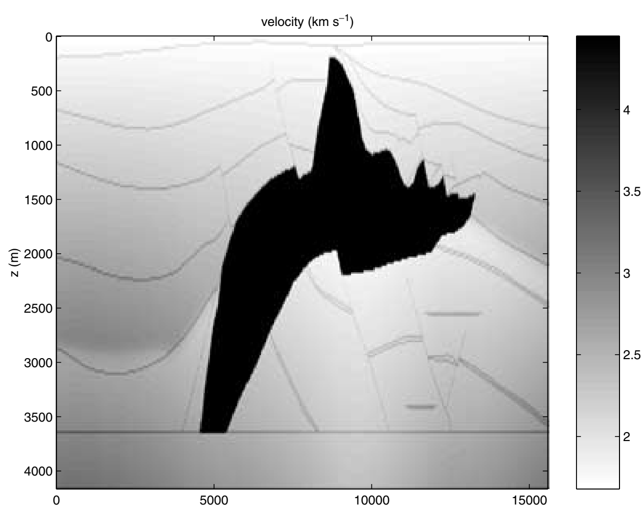

Figure 8. The SEG/EAGE salt dome model.

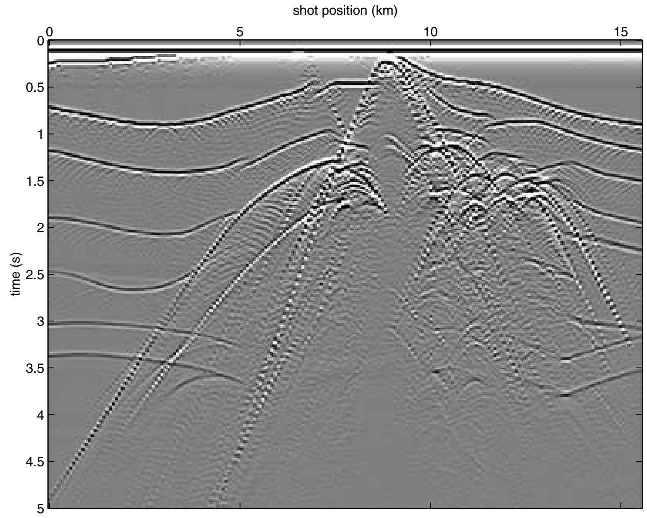

Figure 9. Shortest-offset gather of the salt dome data set.

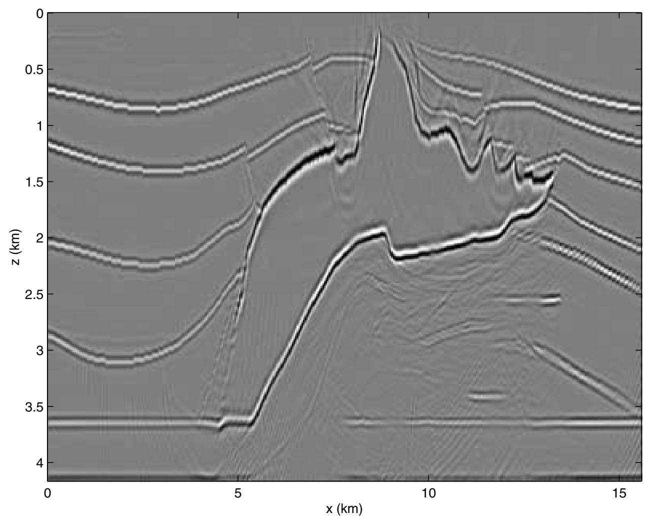

Figure 10. Migrated image obtained with a frequency spacing of 0.3 Hz and the two-way migration code.

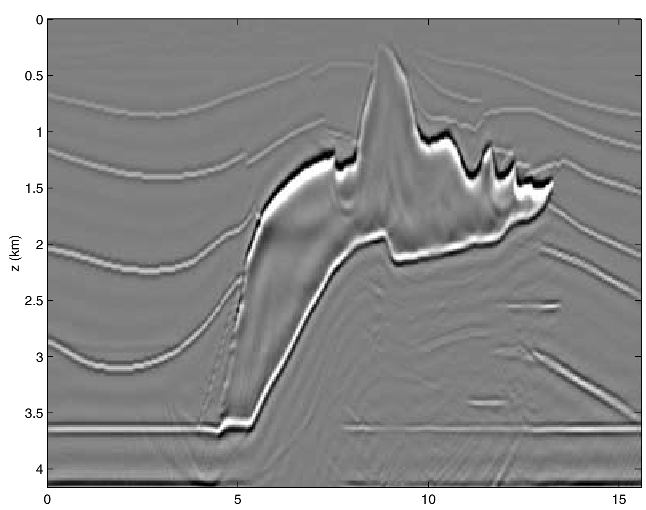

Figure 11. Migrated image obtained with a frequency spacing of 0.3 Hz and the one-way migration code.

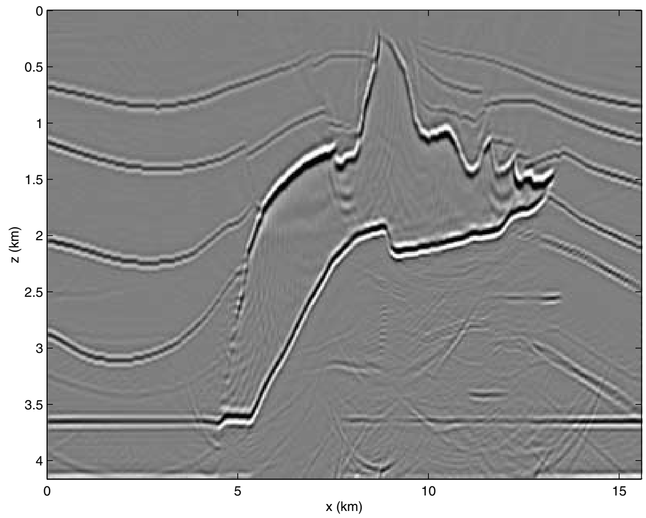

Figure 12. Migrated image obtained with a frequency spacing of 0.5 Hz and the two-way migration code.

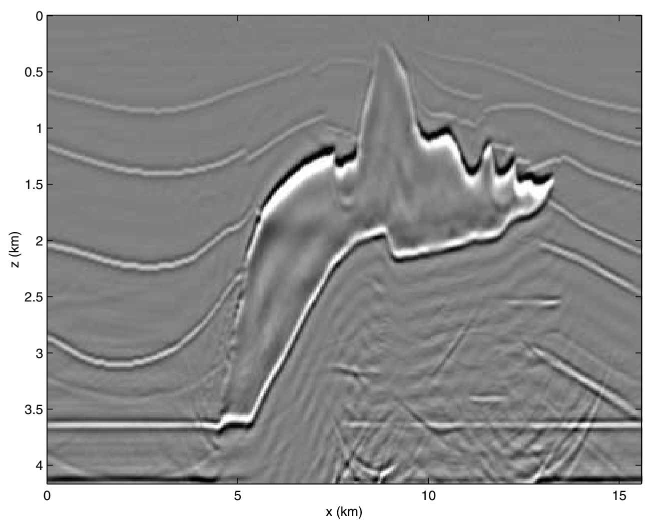

Figure 13. Migrated image obtained with a frequency spacing of 0.5 Hz and the one-way migration code.

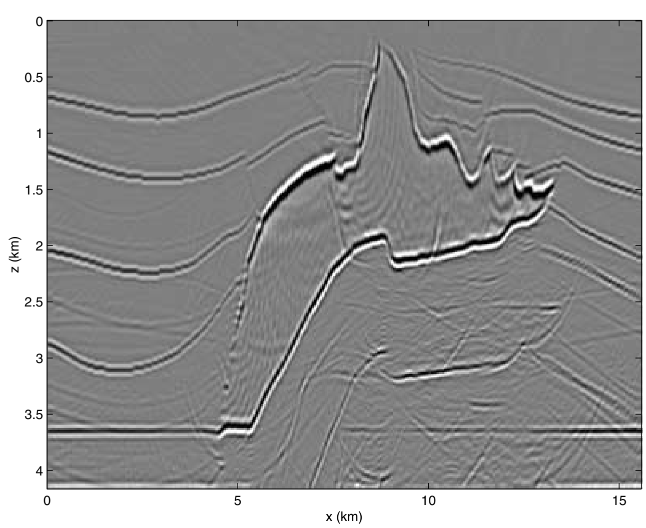

Figure 14. Migrated image obtained with a frequency spacing of 1.0 Hz and the two-way migration code.

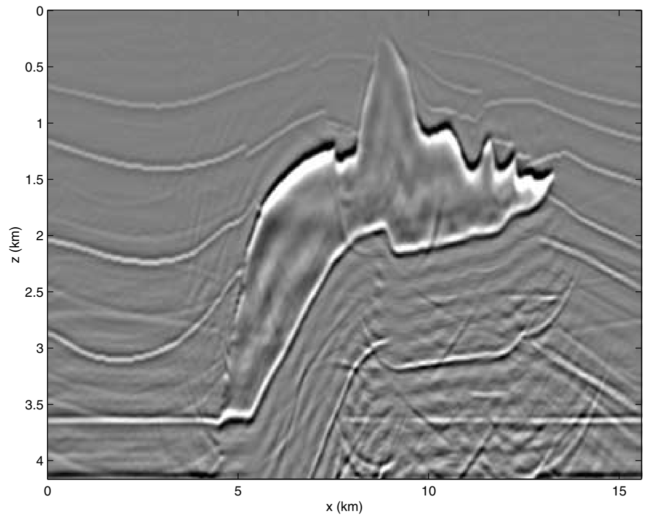

Figure 15. Migrated image obtained with a frequency spacing of 1.0 Hz and the one-way migration code.

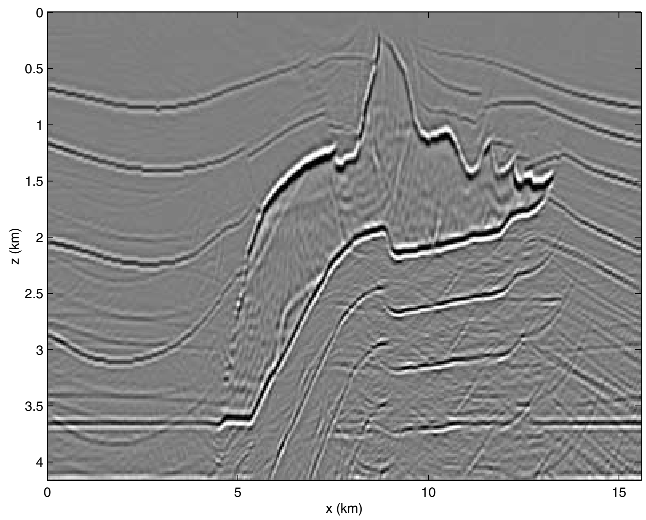

Figure 16. Migrated image obtained with a frequency spacing of 2.0 Hz and the two-way migration code.

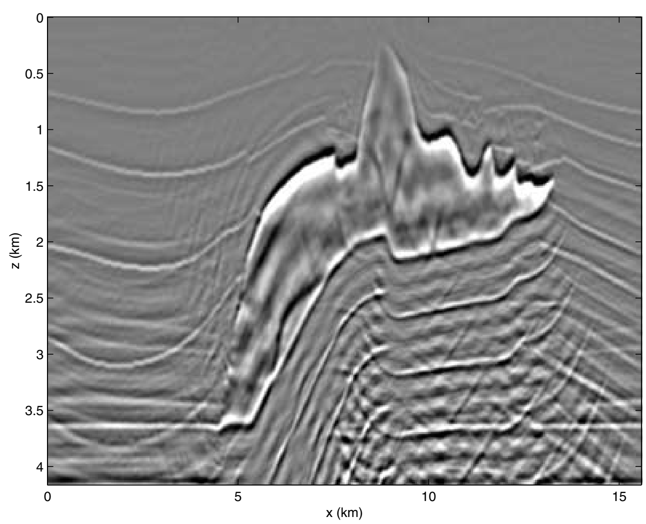

Figure 17. Migrated image obtained with a frequency spacing of 2.0 Hz and the one-way migration code.

This example shows that the conditions on the frequency sampling provides useful estimates also for non-constant-velocity models. This condition is applicable for one-way and two-way frequency-domain migrations. It should be noted that the conditions on the frequency spacing found here lead to values that are generally smaller than suggested in Sirgue & Pratt (2001). These authors, however, concentrate on non-linear inversion, which may help to remove artefacts that occur in the first iteration.

4 CONCLUSIONS

This simple study has shown that the frequency spacing should be chosen carefully to avoid wrap-around effects in the migrated images. We have determined conditions on the choice of frequencies to be used in frequency-domain finite-difference migration, assuming noise-free data. The conditions depend on the velocity, depth of the migration grid and offset range. They show that the spacing between subsequent frequencies can be larger than the inverse of the time range prescribed by the Nyquist theorem.

This demonstrates the potential advantage of a frequency-domain approach for finite-difference migration. An order of magnitude can be gained in computational efficiency over time-domain migration in two space dimensions for multishot data sets. This gain is obtained because of the efficient modelling, because only a relatively small number of frequencies are needed and because a coarser computational grid in combination with interpolation can be used for the lower frequencies without an appreciable loss of numerical accuracy.

REFERENCES

Aminzadeh, F., Brac, J. & Kunz, T., 1997. *3-D Salt and Overthrust Models,* Soc. Explor. Geophys., Tulsa, OK, USA.

Beylkin, G., 1985. Imaging of discontinuities in the inverse scattering problem by inversion of a causal generalized Randon transform, *J. Math. Phys.,* **26,** 99–108.

Biondi, B. & Palacharla, G., 1996. 3-D prestack migration of common-azimuth data, *Geophysics,* **61,** 1822–1832.

Bleistein, N., 1987. On the imaging of reflectors in the Earth, *Geophysics,* **52,** 931–941.

Bunks, C., Saleck, F.M., Zaleski, S. & Chavent, G., 1995. Multiscale seismic waveform inversion, *Geophysics,* **60,** 1457–1473.

Claerbout, J.F., 1971. Towards a unified theory of reflector mapping, *Geophysics,* **36,** 467–481.

Collino, F. & Joly, P., 1995. Splitting of operators, alternative directions, and paraxial approximations for the three-dimensional wave equation, *SIAM J. Sci. Comput.,* **16,** 1019–1048.

Docherty, P., 1991. A brief comparison of some Kirchhoff integral formula for migration and inversion, *Geophysics,* **56,** 1164–1169.

Jin, S., Wu, R.S. & Peng, C., 1998. Prestack depth migration using a hybrid pseudo-screen propagator. In: *68th Annual Meeting, SEG, Expanded Abstracts,* pp. 1819–1822, Soc. Explor. Geophys., Tulsa, OK, USA.

Lailly, P., 1983. The seismic inverse problem as a sequence of before stack migration. In: *Proc. of Conf. on Inverse Scattering, Theory and Applications,* pp. 206–220, eds Bednar, J.B., Redner, R., Robinson, E., Weglein, A., SIAM, Philadelphia, PA, USA.

Marfurt, K., 1984. Accuracy of finite-difference and finite-element modelling of the scalar and elastic wave equation, *Geophysics,* **49,** 533–549.

Mulder, W.A. & Plessix, R.-E., 2002. Time- versus frequency-domain modelling of seismic wave propagation. In: *64th Annual Meeting, EAGE, Extended Abstracts,* Abstract No. E015, Eur. Assoc. Explor. Geophys., Houten, the Netherlands.

Plessix, R.-E. & Mulder, W.A., 2002a. How to choose a subset of frequencies for frequency-domain finite-difference migration. In: *64th Annual Meeting, EAGE, Extended Abstracts,* Abstract No. E038, Eur. Assoc. Explor. Geophys., Houten, the Netherlands.

Plessix, R.-E. & Mulder, W.A., 2002b. Amplitude-preserving finite-difference migration based on a least-squares formulation in the frequency domain. In: *72nd Annual Meeting, SEG, Extended Abstracts,* Extended Abstract MIG 4.3, pp. 1212–1215, Soc. Explor. Geophys., Tulsa, OK, USA

Plessix, R.-E. & Mulder, W.A., 2004. Frequency-domain finite-difference amplitude-preserving migration, *Geophys. J. Int.* **157,** 975–987.

Plessix, R.-E., Mulder, W.A. & Pratt, R.G., 2001. Frequency-domain finite-difference migration with only few frequencies? In: *71st Annual Meeting, SEG, Expanded Abstracts,* Extended Abstract MIG P1.2, pp. 1103–1106, Soc. Explor. Geophys., Tulsa, OK, USA.

Pratt, R.G., 1999. Seismic waveform inversion in the frequency domain. Part I: Theory and verification in a physical scale model, *Geophysics,* **64,** 888–901.

Pratt, R.G., Shin, C. & Hicks, G.J., 1998. Gauss-Newton and full Newton methods in frequency-space seismic waveform inversion, *Geophys. J. Int.,* **133,** 341–362.

Shin, C., Jang, S. & Min, D.J., 2001. Improved amplitude preservation for prestack depth migration by inverse scattering theory, *Geophys. Prospect.,* **49,** 592–606.

Sirgue, L. & Pratt, R.G., 2001. Frequency domain waveform inversion—a strategy for choosing frequencies. In: *63rd Annual Meeting, EAGE, Extended Abstracts,* Abstract No. P014, Eur. Assoc. Explor. Geophys., Houten, the Netherlands.

Symes, W.W. & Carazzone, J.J., 1991. Velocity inversion by differential semblance optimization, *Geophysics,* **56,** 654–663.

Tarantola, A., 1984. Inversion of seismic reflection data in the acoustic approximation, *Geophysics,* **49,** 1259–1266.

ten Kroode, A.P.E., Smit, D.-J. & Verdel, A.R., 1998. A microlocal analysis of migration, *Wave Motion,* **28,** 149–172.

Wu, R.S., 1994. Wide-angle elastic wave one-way propagation in heterogeneous media and an elastic wave complex-screen method, *J. geophys. Res.,* **99,** 751–766.

Xu, S. & Lambaré, G., 2000. 3D migration/inversion in complex media: application to SEG/EAGE salt model. In: *62nd Annual Meeting, EAGE, Extended Abstracts,* Abstract No. C-52, Eur. Assoc. Explor. Geophys., Houten, the Netherlands.